Analyzing highly uncertain source regions in the Ex-UTLS and their effects on small-scale atmospheric composition using probabilistic retroplume calculations

Annika Vogel[a,b,*], Jörn Ungermann[c], Hendrik Elbern[b]

[a] *Institute for Energy and Climate Research - Troposphere (IEK-8), Forschungszentrum Jülich, Germany*
[b] *Rhenish Institute for Environmental Research at the University of Cologne, Germany*
[c] *Institute for Energy and Climate Research - Stratosphere (IEK-7), Forschungszentrum Jülich, Germany*

Abstract

Forecasts of atmospheric composition in the Ex-UTLS (extratropical upper troposphere – lower stratosphere) are highly sensitive to uncertainties in the source regions of air masses. This study investigates the reliability of calculated source regions and their effects on trace gas distributions in this region. For this purpose, an ensemble-based probabilistic retroplume approach is developed to track source regions of air masses. This approach provides the ability to account for both, (i) the contribution of different source regions to an air mass by adjoint diffusion and (ii) the uncertainty of theses source regions with respect to forecast dynamics. Probabilistic retroplume calculations are applied to an air mass in the vicinity of a weak saddle-point in the Ex-UTLS in order to investigate its effect on source regions. The results indicate high sensitivity of source regions to uncertainties in atmospheric transport revealed by perturbed meteorological forecasts. Additionally considering the sources of surrounding air masses leads to even larger spread of source regions. Spreading over large parts of Europe and altitudes between 8 and 14 km within two days, probable source regions comprise completely opposite transport-directions. This large uncertainty of source regions show significant effect on atmospheric composition in the vicinity of the

*Corresponding author
Email address: av@eurad.uni-koeln.de (Annika Vogel)

saddle-point on a short timescale. Evaluating the effect of meteorological uncertainties on local distributions of trace gases, ozone concentrations range from 50 to 350 ppbv at the same location. Probabilistic retroplume calculations suggest a clear connection between these concentrations and related source regions.
Keywords: adjoint sensitivity analysis, source region, uncertainty estimation, atmospheric transport, atmospheric composition, dynamic instability, UTLS

1. Introduction

Trace gas distributions in extratropical upper troposphere - lower stratosphere (*Ex-UTLS*) height levels are dominated by large gradients between stratospheric and tropospheric air masses. This highly variable composition introduces major uncertainties in distributions of atmospheric trace gases caused by tropopause dynamics (see eg. [1] for a theoretical overview).

Observational studies based on airborne measurements of tropopause dynamics were published as early as [2], and many others, where downward movement induced by identified tropopause folding events was given special attention. [3] showed that even small discrepancies in the strength of isentropic mixing can induce large errors in the atmospheric composition of this area. As atmospheric chemical composition has a strong impact on the radiative transfer, the knowledge of trace gas distributions like ozone or water vapor is crucial for the local radiation budget (e.g. [4]). The radiative effect of trace gases is also influencing the local dynamics by thermal effects. This leads to a direct interaction of chemical, thermal and dynamical aspects [5]. In addition, the processes involved cover a large range of spatial and temporal scales, which makes observations as well as modeling of the Ex-UTLS especially challenging.

From a remote sensing perspective, different types of satellites with nadir- and limb-scanning instruments have been launched to remotely sense distributions of atmospheric trace gases on an operational basis (e.g. [6, 7]). However, these instruments are not able to resolve small-scale gradients appearing along air mass boundaries around the tropopause. By performing tomographic obser-

vations, the airborne limb-imaging sensor *GLORIA* (*Gimballed Limb Observer for Radiance Imaging of the Atmosphere*, [4]) has demonstrated its ability to resolve these structures in all three dimensions (e.g. [8, 9]).

Although novel measurement techniques are able to provide observations of the Ex-UTLS with adequate resolution, their spatial and temporal coverage is limited (e.g. [4]). Advanced spatio-temporal data assimilation techniques are able to exploit observations for analyzing dynamically or chemically consistent fields. Among many other algorithms, 4-dimensional variational data assimilation (*4D-var*) is an advanced technique which is widely used in meteorological and chemical forecast systems (e.g. [10, 11, 12, 13]). As a spatio-temporal smoother, 4D-var is able to propagate signals forward and backward in time. This ensures temporal consistency while forcing the model result towards the observations.

Even using advanced assimilation techniques, the model results highly rely on background fields and related uncertainties (e.g. [14]). For initializing ozone fields in the Ex-UTLS, a useful approach exploits conservative dynamical properties of air masses of stratospheric origin. Already [15] observed a high correlation between potential vorticity (PV) and ozone mixing ratios along isentropes in the UTLS. This correlation between a dynamical tracer like PV and an atmospheric gas is not obvious due to different sources and sinks [16]. Nevertheless, practice shows that PV performs well in identifying air masses at the UTLS (e.g. [1, 17, 18, 19, 20]). Furthermore, [21] and [22] demonstrated the potential of combining PV fields with tracer observations to gain an approximation of the chemical state in this region.

However, PV-based initialization of ozone fields makes the chemical forecasts increasingly sensitive to dynamics. Considering the high gradients of PV (and ozone) at the tropopause most notably at the polar vortex edge, local concentration estimates are highly dependent on the air mass forecast. Depending on their source regions, air masses originating from stratospheric or tropospheric regions induce significantly different trace gas distributions. This makes forecasts of ozone fields in the Ex-UTLS highly dependent on transport processes

during the days before. Thus, slight uncertainties in calculated source regions of an air mass may lead to huge differences in local ozone distributions. These uncertainties become especially significant at dynamical instabilities as they appear around the tropopause (e.g. [23]).

Usually, the source locations of an air mass are approximated by backward-trajectories. Due to its low computational effort, this approach is widely used for various applications (e.g. [24, 25, 26, 27, 28]). However, tracking the source region of an air mass by a single trajectory does not account for (i) the contribution of different source regions to an air mass and (ii) the uncertainty of theses source regions with respect to simulated dynamics. The sensitivities to uncertain dynamical forecasts are aggravated by critical flow patterns [29]. Even under highly idealized conditions of two dimensional flow fields with multiple vortices, efficient mixing from different regions can be demonstrated theoretically (e.g. [30, 31, 32]). In case of four vortices systems, the behavior can even be chaotic (e.g. [33, 34]).

In some studies, processes which are related to deformation and wind shear are simulated by backward-trajectories started from slightly displaced locations (e.g. [35, 36]). Other approaches include the use of stochastic simulations for unresolved turbulence or multi-model ensembles with different wind fields and trajectory algorithms (e.g. [36]). Nevertheless, [37] adjudicates that the physical representation of atmospheric diffusion still remains disregarded which limits its application for example in atmospheric emergency scenarios. Possibly for this reason, [23] could not specify the mixing process of observed tropospheric and stratospheric air in the vicinity of a saddle-point.

As an alternative, adjoint formulations of tangent linear models provide the opportunity to transport signals backward in time. These adjoint model formulations are commonly implemented into spatio-temporal data assimilation systems for adjoint source identification (e.g. [38]). The physical description of atmospheric transformations like advection and diffusion renders this approach suitable for analyzing dynamical and chemical processes in the atmosphere (e.g. [39]). Besides this, the adjoint model can be used for estimations of atmospheric

source regions. By taking into account adjoint diffusion processes, these retroplume (or backward plume) calculations provide information on the contribution of different source regions. However, retroplume calculations are sensitive to uncertainties in atmospheric dynamics as well as model description and numerics (e.g. [26]).

This study investigates uncertainties of calculated source regions including the confluence and mixing of different airmasses in the Ex-UTLS using a probabilistic retroplume algorithm. Based on this, related effects on simulated ozone distributions in the local surrounding are investigated. Section 2 gives an overview about the EURAD-IM modeling system including the implemented retroplume algorithm as well as the simulation setup for this case study. The uncertainty analysis of source regions by probabilistic retroplume calculations and its effect on ozone distributions are presented in section 3. Finally, section 4 concludes this study with a discussion of the results including an outlook.

2. Modeling System

The model description in section 2.1 gives the current configuration of the system as well as new implementations for this study. Section 2.2 gives an overview of the model setup and the selected case study.

2.1. Model Description

The *EURAD-IM* (*EURopean Air pollution Dispersion – Inverse Model*) model combines a state-of-the-art chemistry transport model (*CTM*, section 2.1.1) with four-dimensional variational data assimilation (*4D-var*, section 2.1.2). Driving meteorological fields are simulated by the numerical weather prediction model *WRF-ARW* (*Advanced Research WRF*, e.g. [40]). In this study, meteorological initial- and boundary conditions for WRF are taken from global simulations from NOAAs global forecast system (GFS).

New implementations for this study, namely flow-dependent background error correlations and retroplume calculations are described in section 2.1.2 and 2.1.3, respectively.

2.1.1. Chemistry Transport Model

The Eulerian multiscale CTM EURAD provides prognostic calculations of a large number of reactive trace gases and aerosols taking into account dynamical as well as chemical effects [41]. In its general form, the prognostic equation for the concentration c_l of a chemical compound l can be written as:

$$\frac{\partial c_l}{\partial t} = \mathcal{M}_l(\mathbf{c}) + E_l - D_l(c_l) \tag{1}$$

Where E_l and D_l are the source and sink terms of each species c_l, respectively. The nonlinear model operator $\mathcal{M}_l(\mathbf{c})$ consists of dynamical and chemical conversions, where $\mathbf{c}$ denotes the vector of all trace gases c_l. Its implementation is based on symmetric operator splitting to account for the interaction of the different processes:

$$\mathcal{M} = \left[\mathcal{D}_h^{\frac{1}{2}}\ \mathcal{T}_h^{\frac{1}{2}}\ \mathcal{T}_v^{\frac{1}{2}}\ \mathcal{D}_v^{\frac{1}{2}}\right] \mathcal{C} \left[\mathcal{D}_v^{\frac{1}{2}}\ \mathcal{T}_v^{\frac{1}{2}}\ \mathcal{T}_h^{\frac{1}{2}}\ \mathcal{D}_h^{\frac{1}{2}}\right] \tag{2}$$

Here, horizontal (h) and vertical (v) components of the nonlinear diffusion ($\mathcal{D}$) and advection ($\mathcal{T}$) operators are treated sequentially. The upper index $\frac{1}{2}$ denotes a half model time step Δt. The chemistry module $\mathcal{C}$ applies a 2nd order Rosenbrock scheme with internal adaptive time stepping. The gas-phases chemistry module implemented in EURAD is based on the RACM mechanism including more than 70 chemical species and 230 reactions [42]. Additionally, modal aerosol dynamics are considered by the MADE aerosol module [43].

2.1.2. Chemical Data Assimilation

In the chemical data assimilation system EURAD-IM, the spatio-temporal four-dimensional variational data assimilation algorithm (*4D-var*) is implemented in a preconditioned formulation. According to [44], the costfunction $J(\vec{v}_0)$ and its gradient $\nabla_{\vec{v}_0} J(\vec{v}_0)$ with respect to initial conditions are given by:

$$\begin{aligned} J(\vec{v}_0) &= \frac{1}{2} \cdot \vec{v}_0^T\ \vec{v}_0 + \frac{1}{2} \cdot \sum_{i=0}^{n_{\text{time}}} \left[\left(\mathcal{H}\big(\mathcal{M}_{0,i}(\mathbf{B}^{\frac{1}{2}}\ \vec{v}_0)\big) - \vec{d}_i \right)^T \mathbf{R}^{-1} \left(\mathcal{H}\big(\mathcal{M}_{0,i}(\mathbf{B}^{\frac{1}{2}}\ \vec{v}_0)\big) - \vec{d}_i \right) \right] \\ \nabla_{\vec{v}_0} J(\vec{v}_0) &= \vec{v}_0 + \sum_{i=0}^{n_{\text{time}}} \left[\mathbf{B}^{\frac{T}{2}}\ \mathbf{M}_{0,i}^T\ \mathbf{H}^T\ \mathbf{R}^{-1} \left(\mathcal{H}\big(\mathcal{M}_{0,i}(\mathbf{B}^{\frac{1}{2}}\ \vec{v}_0)\big) - \vec{d}_i \right) \right] \end{aligned} \tag{3}$$

where the optimization variable $\vec{v}_0 := \mathbf{B}^{-\frac{1}{2}} \left(\vec{x}_0 - \vec{x}_0^b\right)$ and $\vec{d}_i := \vec{y}_i - \mathcal{H}\left(\mathcal{M}_{0,i}(\vec{x}_0^b)\right)$ include the model and observation increment, respectively. The nonlinear model operator $\mathcal{M}_{0,i}$ represents the EURAD CTM as described in above, where $\mathbf{M}_{0,i}^T$ is the adjoint of its tangent linearizion. $\mathcal{H}$ is the possibly nonlinear observation operator, $\mathbf{B}$ and $\mathbf{R}$ are the error covariances for model background and observations, respectively. Iterative minimization of the preconditioned costfunction (Eq. (3)) is performed by the limited-memory BFGS (*L-BFGS*, e.g. [45]) algorithm. For a more detailed description of the EURAD-IM assimilation system, see [11].

In EURAD-IM, spatial background error covariances are implemented using a diffusion approach correlating uncertainties of neighboring locations, where the suitable selected diffusion coefficient κ controls the amount of diffusion via a defined *correlation length*. As in most numerical weather prediction systems, the horizontal correlations are assumed to be isotropic and homogeneous [46] by defining a constant coefficient κ. However, [47] showed that a circular signal in the Ex-UTLS tends to evolve to an elliptic structure given by the leading Lyapunov vectors.

According to this, anisotropic background error correlations at tropopause and lower stratospheric heights were implemented into EURAD-IM for this study. Following the approach of [48], an anisotropic coordinate stretching tensor $\mathbf{S}$ is multiplied to the constant diffusion coefficient $\bar{\kappa}$. Within this tensor, stretching is achieved by local stretching factors s_{stre} rotated towards the shear direction α:

$$\begin{aligned} \kappa_h &:= \bar{\kappa} \cdot \mathbf{S} = \bar{\kappa} \cdot \left[\mathbf{T}\, \widetilde{\mathbf{S}}\, \mathbf{T^T}\right] \\ &= \bar{\kappa} \cdot \left[\begin{pmatrix} \cos(\alpha) & \sin(\alpha) \\ -\sin(\alpha) & \cos(\alpha) \end{pmatrix} \begin{pmatrix} {s_{stre}}^{-1} & 0 \\ 0 & s_{stre} \end{pmatrix} \begin{pmatrix} \cos(\alpha) & -\sin(\alpha) \\ \sin(\alpha) & \cos(\alpha) \end{pmatrix} \right] \end{aligned} \quad (4)$$

The implementation of Eq. (4) creates elliptic stretching and compression of the background error covariances.

2.1.3. Retroplume Algorithm

The 4D-var data assimilation algorithm in EURAD-IM includes the adjoint formulation of the linearized prognostic model $\mathbf{M}^T_{i,i+1}$ (compare section 2.1.2). Its task is to propagate information backward in time taking into account the complete set of linearized atmospheric and chemical processes. Besides using the adjoint model in the context of data assimilation, it is modified to investigate the evolution of an air mass backward in time. For this purpose, chemical conversions are switched-off in order to track the evolution of a passive tracer (e.g. [39]). The remaining elements are the tangent linear advection ($\mathbf{T}$) and diffusion ($\mathbf{D}$) operators, split into horizontal (h) and vertical (v) components:

$$\widetilde{\mathbf{M}}^T_{i,i+1} := \left[\left(\mathbf{D}_h{}^{\frac{1}{2}}\right)^T \left(\mathbf{T}_h{}^{\frac{1}{2}}\right)^T \left(\mathbf{T}_v{}^{\frac{1}{2}}\right)^T \left(\mathbf{D}_v{}^{\frac{1}{2}}\right)^T\right] \left[\left(\mathbf{D}_v{}^{\frac{1}{2}}\right)^T \left(\mathbf{T}_v{}^{\frac{1}{2}}\right)^T \left(\mathbf{T}_h{}^{\frac{1}{2}}\right)^T \left(\mathbf{D}_h{}^{\frac{1}{2}}\right)^T\right] \tag{5}$$

This retroplume operator $\widetilde{\mathbf{M}}^T_{i,i+1}$ for a single time step can be used to calculate source regions of an air mass at a chosen location. Let $\gamma_k(i_k)$ be a unit input-signal at the location of the air mass (x_k, y_k, z_k) and zero elsewhere. For each selected air mass $k \in [1, N_k]$, the source region is calculated by applying the input-signal $\gamma_k(i_k)$ to the retroplume operator $\widetilde{\mathbf{M}}^T_{i,i_k}$ at time step i_k:

$$\gamma_k(i) = \widetilde{\mathbf{M}}^T_{i,i_k}\ \gamma_k(i_k) = \left(\widetilde{\mathbf{M}}^T_{i,i+1} \circ \cdots \circ \widetilde{\mathbf{M}}^T_{i_k-1,i_k}\right)\ \gamma_k(i_k) \tag{6}$$

The resulting signal $\gamma_k(i)$ of a past time step $i < i_k$ gives the location and relative importance of source regions for the chosen airparcel. In other words, $\gamma_k(i)$ provides the distribution of air masses at time step i, which will contribute to the air mass at location (x_k, y_k, z_k) at a later time step $i_k > i$.

2.2. Simulation Setup

The simulations in this study are performed in four steps. Firstly, meteorological forecasts are performed by the numerical weather prediction model WRF-ARW. Secondly, chemical forecasts are performed by the chemical transport model EURAD. Thirdly, high-resolution remote sensing observations are assimilated into the chemical data assimilation system EURAD-IM providing an

chemical analysis for validation. Finally, probabilistic source areas of selected air masses are simulated by an ensemble of retroplume calculations.

For all simulation steps, both model domains are set up with identical grid points, except an embedding 1 grid point extension of the meteorological grid. The horizontal grid applies an Arakawa-C grid stencil. The domain encompasses the European continent and eastern North Atlantic with a uniform horizontal resolution of 15 km, applying a Lambert conformal projection. With central tangent point at $54.0°N$ and $12.5°E$, the horizontal dimension of the domain in WRF is 287×347, which reduces to 286×346 for EURAD-IM. The vertical model layers are defined by terrain-following σ-coordinates, where 33 σ-levels are defined in both models, ranging from the surface up to 70 hPa. With the study focus placed on the tropopause height levels, the mid tropospheric vertical resolution of 1500 m was refined down to 600 m in the Ex-UTLS. While the time step for WRF is 30 seconds, a larger time step of 300 seconds was selected for EURAD-IM for computational reasons.

An introduction to the case study is given in section 2.2.1. The setup of the meteorological ensemble is described in section 2.2.2 and the EURAD-IM model setup is given in section 2.2.3. The performance of both, meteorological and chemical ensemble forecasts are evaluated against an analysis as described below.

2.2.1. Selection of Case Study

Saddle-points are a famous example of large-scale dynamical instabilities in the upper troposphere. The flow deformation induced by converging and diverging branches creates highly complex motions and trace gas distributions [23]. Due to large local gradients in the UTLS, high-resolution observations around saddle-points are required for validation purposes. On 26.09.2012, airborne observations from the GLORIA instrument provide three-dimensional trace gas distributions at a saddle-point in the Ex-UTLS [49]. These observations provides an unprecedented basis for validating model results and related uncertainties.

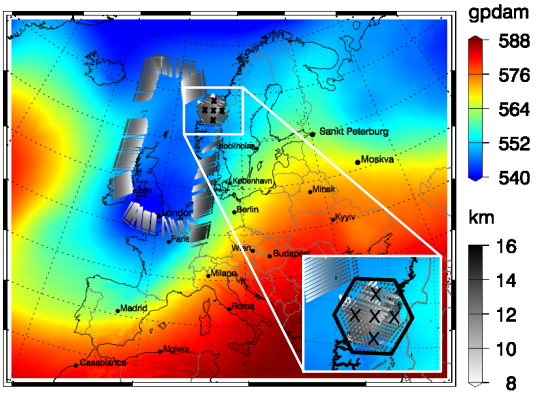

Figure 1: Geopotential height at 500 hPa on 26.09.2012 at 12 UTC from meteorological analysis (coded by colors). Tangent points of GLORIA ozone retrievals are indicated in gray colors (coded by altitude). Small black crosses at the hexagonal observation indicate analyzed *target points*. The hexagonal flight path is scratched as black hexagonal in the lower right inlet.

The synoptic situation on this day was dominated by a trough over north-western Europe causing a meridional circulation over the North Atlantic and Europe. As shown in Figure 1, the trough's axis is orientated on the southwest-northeast direction reaching from the Norwegian coast until north-western Spain. The pressure minimum in the trough's center originates from a cut-off system which is partly reconnected to the polar vortex. Nevertheless, a closed circulation around the center above the British Islands is still present at this time. In case of closed circulations, a hyperbolic- or saddle-point is located at its edge to the polar vortex where converging- and diverging flow pattern coexist (compare [23]).

Available GLORIA observations cover the trough's boundary (above north-western Germany), its center (above the British Islands) as well as its connection to the polar vortex (between Iceland and Norway). At the latter, the airplane flew an hexagonal flight pattern allowing three-dimensional tomographic observations between 8 and 14 km altitude above the coast of Norway (see [49]). The location of this *hexagonal observation*, which was observed between 11:30 and 13:00 UTC, is expected to be close to the saddle-point inducing highly variable

trace gas distributions around the tropopause.

2.2.2. Setup of Meteorological Ensemble

In order to investigate dynamically-induced uncertainties of source regions, a meteorological ensemble is used to provide probabilistic dynamical forecasts. Probabilistic forecasts from the operational global GFS ensemble (*GEFS*, e.g. [50]) provided by NCEP are used to drive an ensemble of WRF simulations via initial- and boundary conditions. The WRF simulations were initialized on 24.09.2012 - two days before the day of interest - at 00 UTC to allow the perturbations to evolve in time.

From this meteorological ensemble, a subset of four members is selected for the uncertainty analysis (section 3). Besides the WRF forecast based on the GEFS control run (= member 1), forecasts driven by GEFS member p03 (= member 2), p09 (= member 3) and p10 (= member 4) are selected for this case study. The selection is made upon the largest variations in the Ex-UTLS at the day of interest.

The probabilistic meteorological forecasts are validated by a WRF simulation based on the daily GFS analysis. Three single-day-forecasts are performed by WRF, each driven by the latest GFS analysis at 00 UTC. These daily forecasts were stringed together to give a meteorological analysis for this three days. It should be noted, that reinitialization of WRF by the daily GFS analysis may result in inconsistencies between dynamical fields and ozone. More specifically, we argue that these discontinuities are less detrimental for the analysis than the grown-up forecast error of a single 3-day simulation. Consequently, the difference in ozone because of reinitialization are assumed to be smaller than the errors in ozone due to grown-up dynamical forecast errors. Hence, for the purpose of this study, it is an efficient way in producing a meteorological analysis which sufficiently approximates the true state.

2.2.3. Setup of EURAD-IM

Meteorological and chemical forecasts for this study were performed starting two days before the day of interest. Thus, the simulation period is 24.09.2012, 00 UTC until 26.09.2012, 16 UTC for the probabilistic forecast of both models. The chemical ensemble is created by a set of forecast of EURAD-IM each driven by a different member of the meteorological ensemble (see section 2.2.2).

For validation of the uncertainties in atmospheric composition on 26.09.2012, the chemical forecast for this day is driven by the meteorological analysis. Additionally, high-resolution ozone-retrievals from GLORIA are assimilated to improve the chemical analysis with respect to the observations. The assimilation-window from 06 to 16 UTC on 26.09.2012 was chosen to cover all available GLORIA observations.

Focusing on upper tropospheric ozone distributions, the aerosol dynamics within EURAD-IM are switched-off for this study to reduce the computational costs. The use of retroplume calculations for the approximation of source regions is highly sensitive to spurious oscillations in the advection algorithm. The Walcek advection scheme [51] is selected because of its high monotonicity during the retroplume calculations.

Although the EURAD-IM model system covers atmospheric processes up to the stratosphere, it is mostly used for lower tropospheric applications (e.g. [11]). Therefore, some modifications are undertaken to improve its representation around the tropopause. For this study, the top of the model is lifted from 100 hPa to 50 hPa. Additionally, the number of vertical layers is increased in order to ensure a vertical resolution of about 250 m around the tropopause.

Furthermore, fields of potential vorticity (PV) are used for ozone initialization and anisotropic background error correlations (BEC). Assuming PV to be approximately a conservative tracer for the times scales of this study, similar PV values can be related to homogeneous air masses in the UTLS (e.g. [1, 52]). Thus, horizontal gradients of PV are used as indicator of air mass boundaries and consequently decreased spatial correlations of chemical composition. Fol-

lowing the approach of [48], horizontal gradients of PV are used for direction (α) and amount (s_{stre}) of stretching in the BECM (compare section 2.1.2).

Although the general correlation between PV and ozone is well known since decades, the concrete factor for relating ozone to PV has to be approximated for each specific situation (e.g. [53]). For this study, a correlation factor of $40\ \frac{ppbv}{pvu}$ is used to initialize ozone fields as well as update ozone boundaries during the simulation in the upper troposphere. The high correlation between ozone and PV is only valid for stratospheric conditions, loosing validity below the dynamical tropopause. Thus, PV-based initialization of ozone and anisotropic BEC are only applied to model layers above 6 km altitude.

3. Uncertainty Analysis

This section provides an uncertainty analysis of the upper tropospheric state in presence of a weak saddle-point inside the polar vortex on 26.09.2012. The analysis includes the uncertainty in the location of the saddle-point in section 3.1, the uncertainty of source regions of air masses at the saddle-point in section 3.2 and the uncertainty of local chemical distributions in section 3.3. For each step, the probabilistic forecasts based on the meteorological ensemble are validated by the analysis as describes in section 2.2.

3.1. Uncertainty of Saddle-point

The first step is the evaluation of the meteorological ensemble with respect to upper tropospheric state. Figure 2 shows the ensemble forecasts of geopotential height at 200 hPa on 26.09.2012 at 12 UTC. The large-scale trough over northwest Europe is predicted by all members with little differences in its position and extension. The location of the minimum geopotential height is forecast above the North Sea roughly between Denmark and England. The isolines of geopotential height in Figure 2 give an rough indication on the horizontal circulation at the selected time.

In case of closed circulation patterns, saddle-points occur where an isoline just separates into two disjoint isohypses. On 26.09.2012, the flow around the

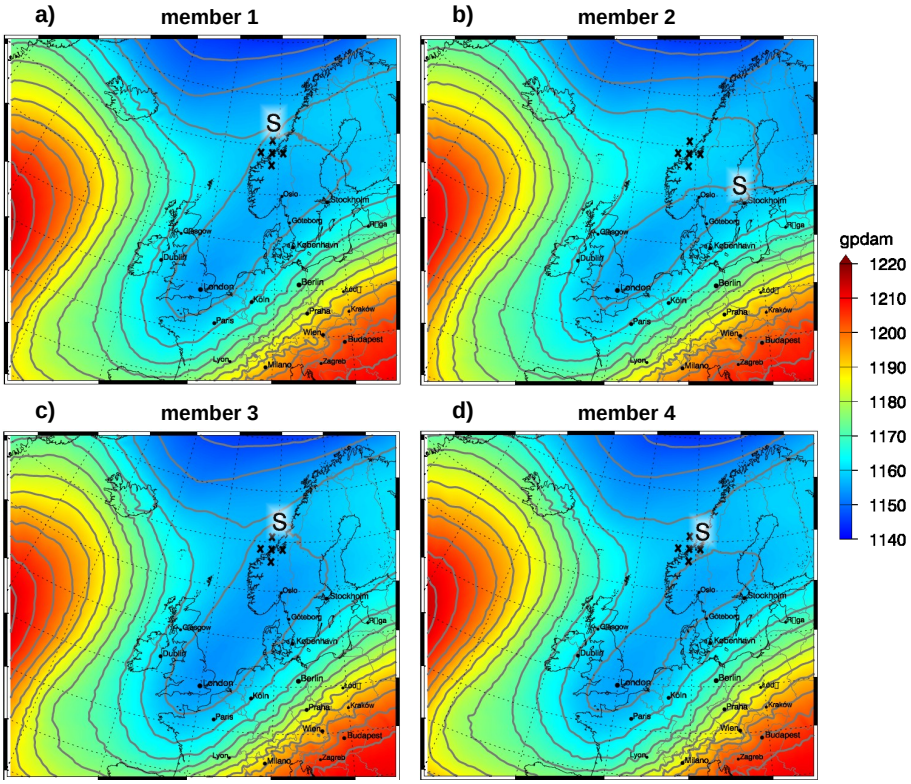

Figure 2: Geopotential height at 200 hPa on 26.09.2012 at 12 UTC. Each subplot shows the forecast of one ensemble member initialized on 24.09.2012 at 00 UTC. Geopotential heights are coded by color (contour) and gray isolines. Target points are given by small black crosses and the position of the saddle-point is indicated by the letter **S**.

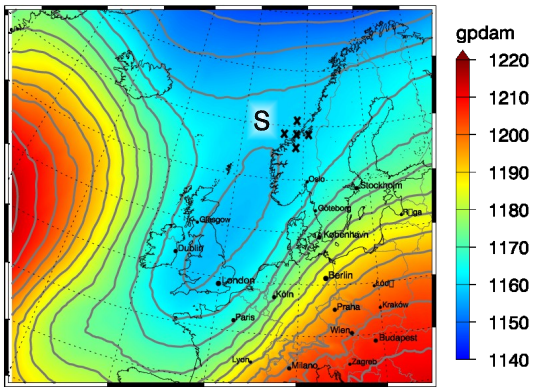

Figure 3: Analysis of geopotential height at 200 hPa on 26.09.2012 at 12 UTC. Geopotential heights are coded by color (contour) and gray isolines. Target points are given by small black crosses and the position of the saddle-point is indicated by the letter **S**.

trough is separated from the polar vortex forming a weak saddle-like shape of geopotential height. Although the trough appears to be forecast accurately by the ensemble, the location of the saddle-point differs significantly. Its location at 200 hPa varies from the coast of Norway (member 3) to close to Stockholm (member 2). Thus, forecasting the exact location of a saddle-point is considered to be highly sensitive to perturbations in the large-scale dynamics.

The uncertainty indicated by the meteorological ensemble is validated by the meteorological analysis. The analysis of geopotential height in 200 hPa is given in Figure 3. As indicated by the small ensemble-spread, the analyzed extension of the trough over western Europe was sufficiently well predicted by forecasts. Compared to the ensemble forecasts, the trough's axis is slightly shifted to the west in the analysis. Thus, the analyzed saddle-point is located west of Norway above the North Sea.

3.2. Uncertainty of Source Regions

The effect of large-scale meteorological uncertainties on source regions of air masses in the vicinity of a weak saddle-point is analyzed. The region of interest is an air volume of about 300 km diameter in 10 to 12 km altitude above the Norwegian coast, which was observed by GLORIA from different directions

Table 1: *Target points* (**TP**) of retroplume calculations on 26.09.2012 at 12 UTC

TP	*center*	*west*	*east*	*south*	*north*	*below*	*above*
latitude	**63.4°N**	63.4°N	63.4°N	**62.4°N**	**64.4°N**	63.4°N	63.4°N
longitude	**8.8°E**	**6.8°E**	**10.8°E**	8.8°E	8.8°E	8.8°E	8.8°E
altitude	**11.0 km**	11.0 km	11.0 km	11.0 km	11.0 km	**10.0 km**	**12.0 km**

(hexagonal observation). The size of the air volume lies within the uncertainty of the saddle-point indicated by the ensemble. In order to analyze source regions of this region, ensemble-based probabilistic retroplume calculations of selected air masses are performed. In addition to the center of the hexagonal observation, source regions of six surrounding air masses are calculated as shown in Table 1 (denoted as *target points*, **TP**).

In terms of the investigation of source regions, dynamical instabilities refer to diverging airmasses backward in time which equals converging motions forward in time. Thus, stable and unstable manifolds at a saddle-point as described by [23] has to be exchanged from an inverse viewpoint.

3.2.1. Horizontal Source Regions

Uncertainties in the location of the saddle-point influence horizontal flow patterns at the region of interest. Figure 4 shows the probabilistic temporal evolution of the air mass in the center of the hexagonal observation (TP *center*). During the last hours, the air mass was transported from eastern to northern directions to the TP, depending on the dynamics forecast by each member. Member 2 predicts a source area transported from the north with an increasing westerly component 48 hours before the time of interest. Within the last 24 hours prior to the time of interest, member 1, 3 and 4 predict slow advection from eastern directions. At approximately 24 hours before, the air mass forecast by member 4 converges from western to southern directions leading to a complex sickle-like shape of the source area 36 hours before. Following member 3, the source area stays east of the TP even 48 hours before. Member 1 predicts an elongated shape of the air mass with a significant contribution of air originating

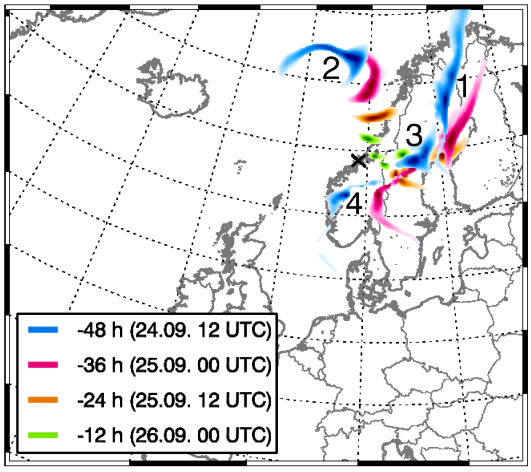

Figure 4: Probabilistic source areas of the air mass at TP *center* (center of the hexagonal observation, compare Table 1) on 26.09.2012 at 12 UTC (black cross). The relative contributions of source areas of each member are indicated by color intensity. Each color gives the distribution of the vertically integrated signal at different times according to the legend. Black numbers attached to the signal 48 hours before (blue contours) indicate the corresponding member number.

from the north. Comparing the source areas predicted by the four members 48 hours before the time of interest, the probabilistic retroplumes demonstrate high uncertainties in the history of the air mass.

As local dynamics may differ significantly within small distance around saddle-points, Figure 5 shows probabilistic source areas for surrounding TPs (compare Table 1). The probabilistic retroplumes indicate a wide range of horizontal source areas 48 hours before the time of interest. Potential source areas are scattered over large parts of north-western Europe within two days. However, source areas of the different members show similar distributions for TPs *center*, *east*, *south* and *below* as well as for TPs *west*, *north* and *above*.

For member 2, the south-eastern position of the saddle-point results in north-western to northern source areas for all considered TPs. For the other members, the saddle-point is located close to region of interest. Highly variable flow around the weak saddle-point has direct influence on the history of the air mass given

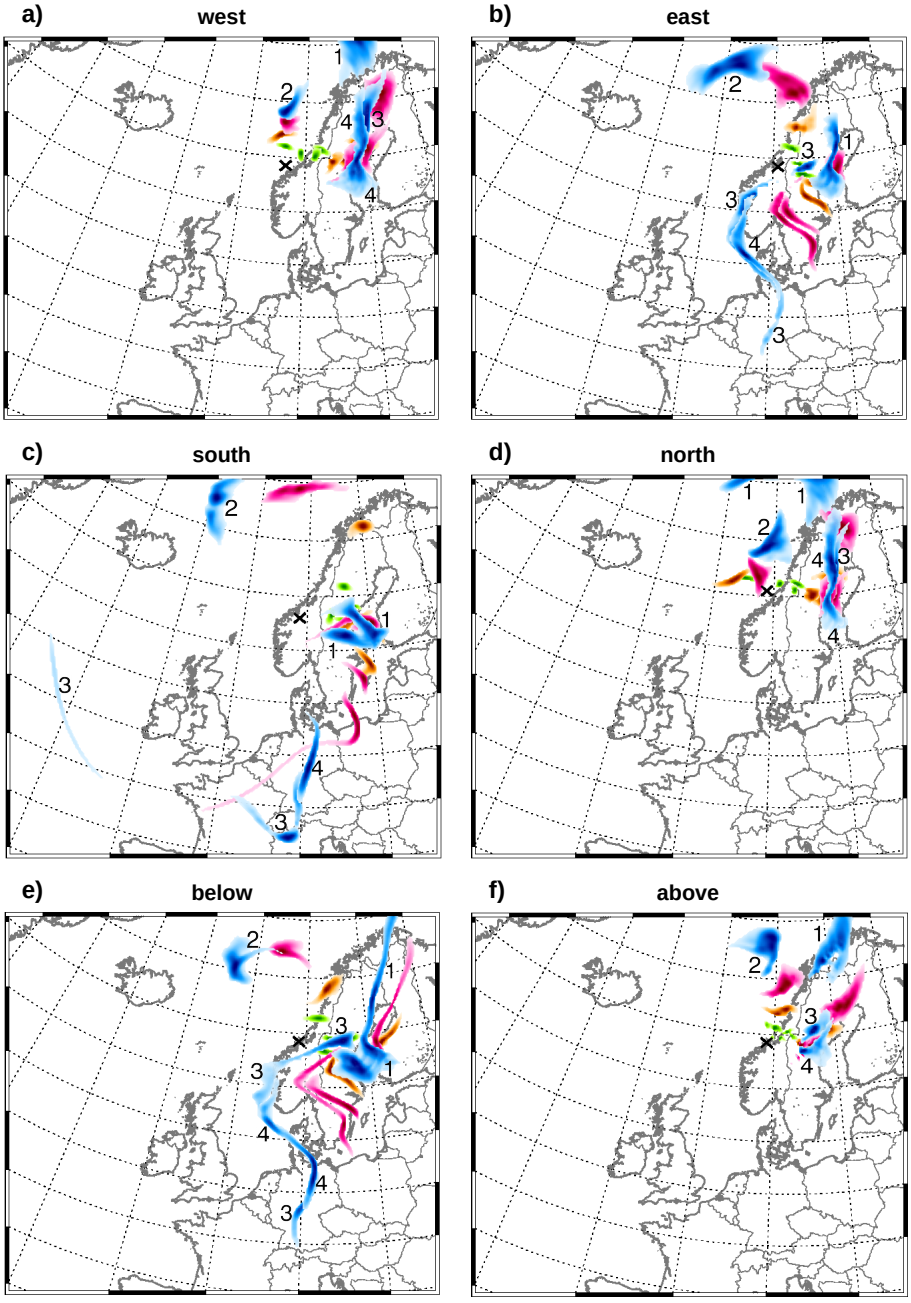

Figure 5: Probabilistic source areas of the surrounding TPs on 26.09.2012 at 12 UTC: (a) TP *west*, (b) TP *east*, (c) TP *south*, (d) TP *north*, (e) TP *below*, (f) TP *above* (black cross, compare Table 1). Plotting conventions as in Figure 4.

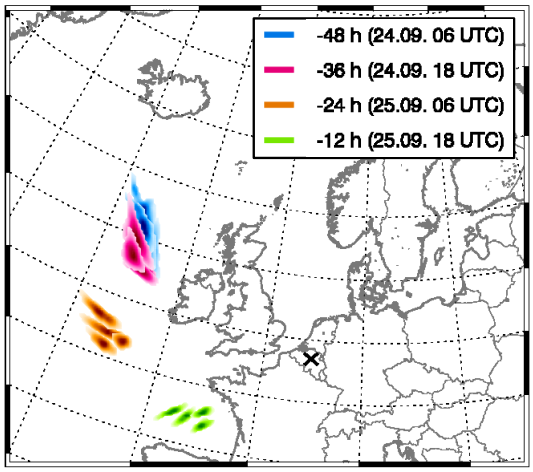

Figure 6: Probabilistic source areas of the air mass at the trough boundary (50.8°N, 4.8°E, 11.0 km a.s.l.) on 26.09.2012 at 06 UTC (black cross). Plotting conventions as in Figure 4.

by diverging source areas.

Taking the surrounding TPs into account, the region of interest may be influenced by air masses originating from large parts of western Europe within 48 hours. Potential source areas range from north-east of Iceland and the Norwegian North Cape in the north over central Sweden and southern Finland in the east to the Alps in the south. This states an even higher uncertainty of source areas of the region of interest compared to the central air mass - indicating complex distributions of trace gases in this region. For TPs *west*, *north* and *above*, probabilistic retroplumes predict slightly less spread of source areas restricted to northern to eastern source directions.

Thus, possible source regions of the airmasses within the hexagonal observation comprise highly diverse or even opposite transport directions. This large uncertainty is caused by the saddle-point as dynamical instability. In contrast, the ensemble of source regions for a TP at the trough's boundary is shown in Figure 6. Not being influenced by any dynamical instability, the air mass was transported along the trough's boundary with a high overlap of the source areas even 48 hours before.

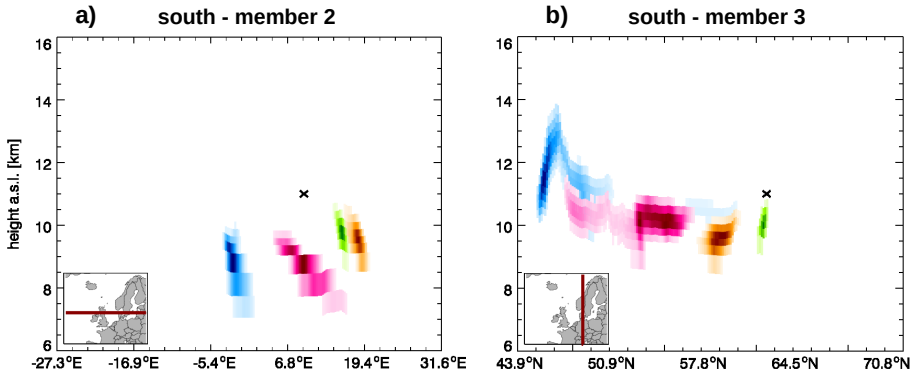

Figure 7: Probabilistic source altitudes at the hexagonal observation from 26.09.2012 at 12 UTC. Shown source altitudes correspond to the southern TP (62.4°N, 8.8°E, 11.0 km a.s.l.) of member 2 (a, in x-direction) and member 3 (b, in y-direction). The temporal evolution of the horizontally integrated source signals are colored by contribution (dark = largest contribution). Colors same as in Figure 5.

3.2.2. Vertical Source Regions

In addition to the horizontal source areas of air masses, their vertical origin also have significant impact on chemical composition. Especially at tropopause height levels, trace gases may differ significantly according to their source altitudes. As an example, Figure 7 shows source altitudes of two members from the TP *south*. This TP appears to have the most diverging source signals in the vertical direction 48 hours before the time of interest. The north-easterly source region of member 2 was lifted from 9 to 10 km height towards 11 km during the last 12 hours - presumably by orographically enforced uplift at the Norwegian coast. Going back to the time span from 36 to 48 hours, source altitudes of 8 to 10 km - with some minor contributions reaching down to 7 km height - are analyzed. These low source altitudes of this member indicate uplift of tropospheric air within the anti-cyclonic flow over Norway.

Upward motion of the air mass is also forecast by member 3 during its advection from south-east during the last 24 hours. However, between 24 and 48 hours before the time of interest, the air mass sinks downwards from higher altitudes. With increasing elongation of the air mass, shearing processes induce

differences in source altitudes. 48 hours before the time of interest, the air mass spreads over altitudes between 10 and 14 km. The highest altitudes can be found over the Alps and may therefore be influenced by orographic effects. A minor source region of member 3 originating from the Atlantic ocean can be found in 10 to 11 km height.

The probabilistic vertical source altitudes can be classified according to the horizontal sources described in section 3.2.1. For most TPs and members, the major contribution of the air mass originates from altitudes between 10 and 12 km at 48 hours before. Northern source areas are mainly related to comparably low altitudes below 10 km (e.g. TP *south* - member 2). Going towards eastern source areas, source altitudes increase to heights of 10 to 13 km east of the TP (e.g. TP *center* - member 3 / TP *west* - member 4). South-western source areas have average altitudes around 11 km with maximum source altitudes of 13 to 14 km induced by downward motions at the Alps and Norwegian mountains (e.g. TP *south* - member 3 / TP *east* - member 3).

3.2.3. Validation of Source Regions

Source regions based on the meteorological analysis for TPs *center* and *north* are given in Figure 8. According to the analyzed source areas, the air mass at TP *center* was transported along the ridge of the trough (compare section 3.1). During the last 24 hours, the air mass was advected from the south to the TP. The cyclonic flow around the trough induces increasing eastward (approx. 36 hours before) and southward advection (approx. 48 hours before) of the air mass. This results in a source area located above the Atlantic Ocean 48 hours before which is highly elongated in the direction of the flow. During this time period, the source area stays narrow in cross-flow direction indicating limited mixing across the boundaries of the trough.

The horizontal stretching of the air mass is connected to vertical shearing processes (Figure 8b). Starting 24 hours before the time of interest, lower parts of the air mass (between 10 and 11 km height) observe higher wind speeds and are faster transported along the trough. Source areas of these lower parts reach

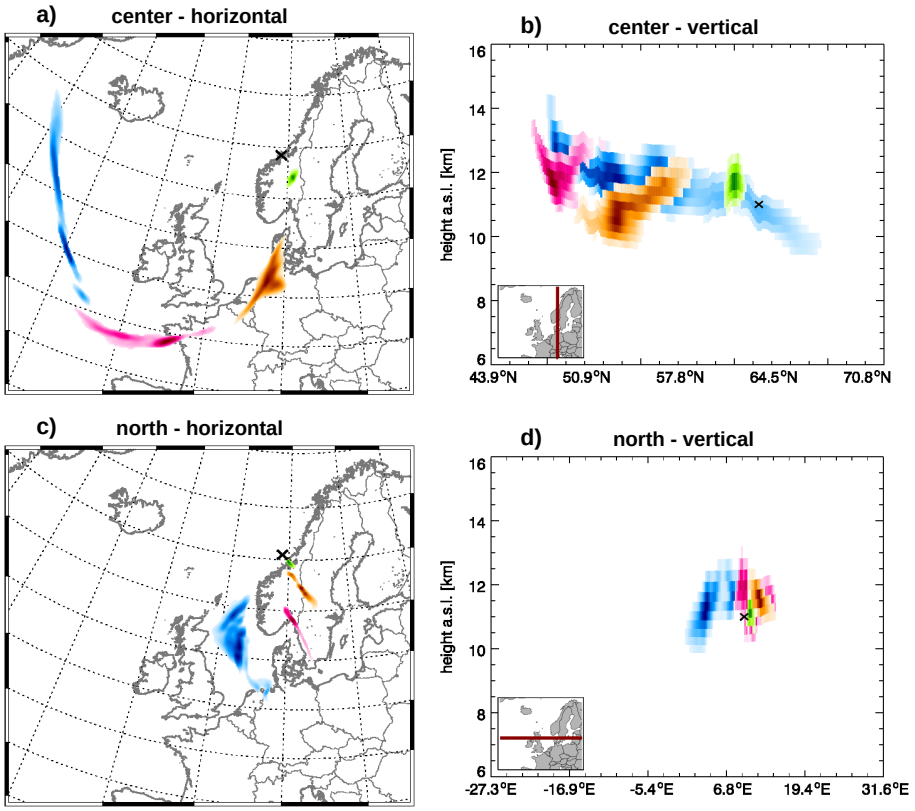

Figure 8: Analysis of source regions on 26.09.2012 at 12 UTC of TP *center* (a,b) and *north* (c,d) in horizontal (a,c) and vertical (b,d) direction (b: y-direction , d: x-direction). Plotting conventions as in Figure 4.

latitudes of 64°N within 48 hours, while higher parts can be found between 52°N and 60°N at this time. The southern edge of the air mass reaches up to 14 km altitude 48 hours before.

The air mass at TP *north* was advected from south-eastern direction towards the TP. While not directly transported along the trough's edge, this air mass observes lower wind speeds and spreads towards larger source areas. Source regions 48 hours before are located at altitudes of 10 to 12 km above the North Sea. Locations *east*, *south*, *above* and *below* have similar source regions as the central TP with larger contributions from lower altitudes for TP *below*. The source region of TP *west* is located between the sources of TPs *center* and *north* (not shown).

Comparing the analyzed source region to the probabilistic forecasts, the horizontal source area of TP *center* was not predicted by the ensemble. Probabilistic source areas 48 hours before the time of interest are located in more easterly regions spread over north-western Europe. Only a small part of the southern air mass of member 3 was transported over the Atlantic ocean at this time (compare Figure 5c). Its location and elongation along the trough's border fits well the analyzed source area of TP *center*. However, the low contribution to the probabilistic source signal indicates low probability of an source area over the Atlantic ocean 48 hours before. The analyzed source region of TP *north* was not predicted by the ensemble at this location. But retroplumes of TPs *east* and *below* indicate contributions of similar source areas over the North Sea.

The differences in source areas between the probabilistic forecasts and the analysis can be explained by large-scale dynamics (compare section 3.1). The region of interest is located close to the weak saddle-point predicted by the meteorological ensemble (except member 2). In the analysis, the position of the trough is shifted westward compared to the ensemble forecasts. Therefore, the region of interest is located on the frontside of the trough, influenced by transport from southern to south-western directions. In this case, the region is not directly influenced by the saddle-point during the 48 hours considered, as indicated by the ensemble forecast.

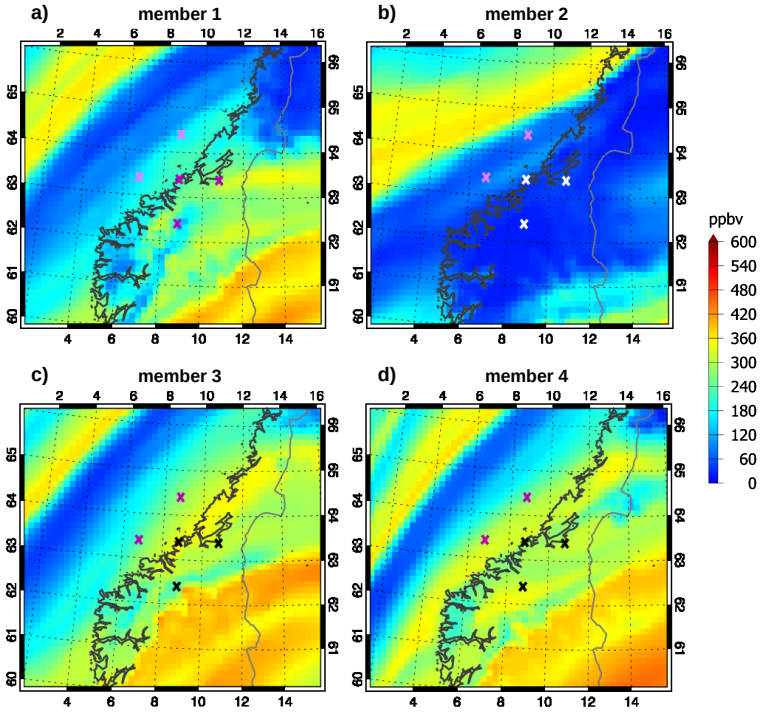

Figure 9: Regional horizontal ozone-distributions of ensemble on 26.09.2012 at 12 UTC. Each subplot shows the forecast of one ensemble member. Ozone mixing ratios are coded by color (contour). TPs are indicated by small crosses, colored according to the source area classification (white: north-west, magenta: north, purple: east, black: south).

3.3. Uncertainty of Chemical Fields

In this section, the effect of highly uncertain source regions to local ozone distributions is evaluated. Probabilistic horizontal- and vertical distributions of ozone are described in section 3.3.1. The validation of the probabilistic forecast with meteorological and chemical analysis is provided in section 3.3.2.

3.3.1. Probabilistic Chemical Fields

The ensemble variability of horizontal ozone concentrations in the surrounding of the TPs is shown in Figure 9 All ensemble members indicate a filament with concentrations below 150 ppbv orientated in south-western to north-eastern direction. Position and extension of the filament differs between the members.

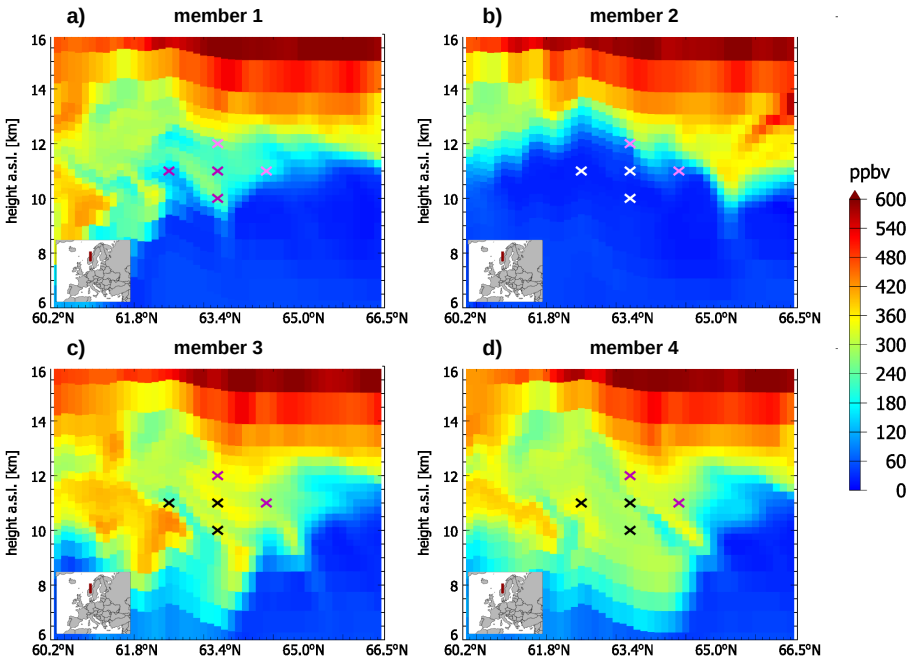

Figure 10: Ensemble of vertical cross sections at hexagonal observation on 26.09.2012 at 12 UTC in y-directions. Each subplot shows the ozone forecast of one ensemble member. Ozone mixing ratios are coded by color (contour). TPs are indicated by small crosses, colored according to the source area classification (white: north-west, magenta: north, purple: east, black: south).

It is most pronounced for member 2 where it covers large parts of the displayed area including all TPs. For the other members, the filament is much thinner and shifted towards north-west. Instead, these members predict medium ozone concentrations between 100 and 400 ppbv at the region of interest. Additionally, comparably high concentrations of about 400 ppbv are forecast by these members in the south-eastern part.

Looking at the vertical cross sections in Figure 10, the local mixing of different air masses becomes visible. The ensemble forecasts show complex structures of tropopause folding with highly varying ozone concentrations in the target region. For member 2, tropospheric ozone concentrations below 100 ppbv extend up to 12 km height. However for the other members 1, 3 and 4, vertical exchange

Table 2: Ensemble statistics of ozone concentrations at TPs (26.09.2012 12 UTC, compare Table 1) and at the trough's boundary (50.8°N, 4.8°E, 11.0 km a.s.l.,26.09.2012 06 UTC, compare section 3.2.1). The ensemble of ozone concentrations, their mean μ and standard deviation σ are given in *ppbv*. The relative uncertainty is given by σ/μ.

	mem 1	mem 2	mem 3	mem 4	μ	σ	σ/μ
center	213.99	52.81	342.85	289.59	224.81	126.27	56.2%
west	158.29	82.76	236.00	309.84	196.72	97.98	49.8%
east	280.09	47.72	299.28	308.79	233.97	124.74	53.3%
south	134.57	19.33	233.53	315.64	175.77	127.89	72.8%
north	173.11	79.81	275.71	271.28	199.98	93.06	46.5%
trough boundary	333.16	361.22	350.87	365.39	352.66	14.36	4.0%

processes are influencing the whole region of the TPs down to 7 km. For these members, enhanced tropopause folding processes can be found in the southern part (left hand side in Figure 10). Consequently, significant downward transport of stratospheric air in this region leads to high ozone concentrations of about 400 ppbv. While for member 1 and 4, the TPs are not directly effected by this air mass, its extension for member 3 reaches close to the TP *south*. Therefore, the retroplume calculations of TP *south* for member 3 (compare section 3.2.2) shows contributions of source altitudes up to 14 km height 48 hours before.

In the following, the local ozone concentrations and the source regions analyzed above are comprised. It is expected that specific concentrations are caused by common source areas - irrespective of the TP and member. Figure 11 shows the source areas for all members and all TPs in 11 km altitude, color coded by the local ozone concentrations at the TP. The concentrations are listed in in Table 2. Assuming conservative transport of ozone, the following general patterns are found:

A Tropospheric air mass: very low concentrations (< 100 ppbv, dark blue colors) are induced by uplift within anti-cyclonic rotated air mass from north-west (TPs *center*, *west*, *east*, *south*, *north*, *below*: member 2)

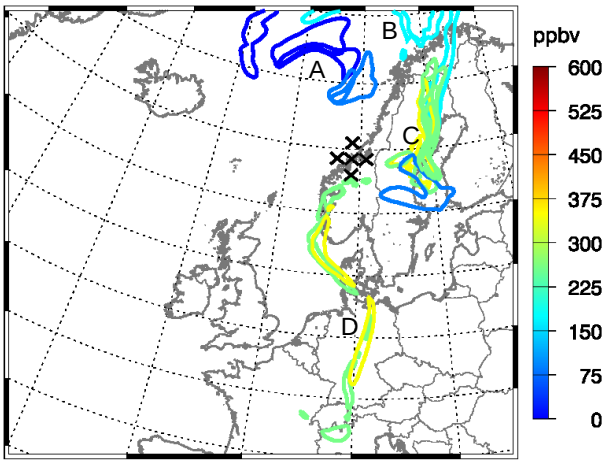

Figure 11: Probabilistic source areas of five air masses (*center*, *west*, *east*, *south*, *north*, compare Table 1) on 26.09.2012 at 12 UTC (black crosses). For each member and TP, the vertically integrated retroplume signals 48 hours before are indicated by isolines. The isolines are colored according to the forecasted ozone concentration at the TPs on 26.09.2012 at 12 UTC (compare Figure 9).

B Mainly tropospheric air mass: low concentrations (100 to 200 ppbv, light blue colors) are induced by northern source areas (TPs *west*, *north*, *above*: member 1 / TP *above*: member 2)

C Mainly stratospheric air mass: medium concentrations (200 to 300 ppbv, green colors) are induced by slow transport from the east (TPs *center*, *east*, *south*, *below*: member 1 / TPs *west*, *north*, *above*: member 3 + 4)

D Stratospheric air mass: high concentrations (> 300 ppbv, yellow colors) are induced by advection from southern to south-western directions connected to downward motion from higher altitudes (TPs *center*, *east*, *south*, *below*: member 3 + 4)

Note that the concentration intervals given for each class **A**-**D** are rough estimations for concentrations at the TPs in 11 km height.

Member 2 predicts very low concentrations (below 50 ppbv) for TPs *center*, *east*, *south* and *below*. Related air masses were transported anticyclonic towards the TPs connected to uplifting motions from altitudes between 8 and 11 km. In

contrast, northern source areas are related to source altitudes of about 11 km and slightly higher ozone concentrations of 50 to 100 ppbv.

For TP *center*, member 1 predicts concentrations around 200 ppbv which are induced by a northern to north-eastern source area. Thus, this TP shows intermediate properties between tropospheric and stratospheric air masses.

In two cases, the relation of source area and resulting ozone concentrations differs from the classification provided above. For member 1 and 3, a thin filament of lower concentrations is forecasted at TP *south* (compare Figure 9). The small-scale uplift of this filaments may not have been captured by the linearized retroplume operator. Instead, the calculated source regions are likely representative for the surrounding air masses connected to higher concentrations (200-300 ppbv for member 1 / >300 ppbv for member 3). Therefore, the two cases are classified according to the surrounding air masses.

Finally, the effect of highly uncertain atmospheric transport on local distributions of trace gases may be quantified by ensemble statistics. Although an ensemble of four members does not provide a sufficient sample size, the statistics in Table 2 give some indication on concentration uncertainties. As example for the hexagonal observation, the ensemble of ozone concentrations at TP *center* indicates a mean concentration of 224.81 *ppbv* with a standard deviation of 126.27 *ppbv*. From this, the relative uncertainty at the TP can be approximated to be 56.2% which is comparable to the surrounding TPs ranging from 46.5% (TP *north*) to 72.8% (TP *south*). This huge uncertainty of ozone concentrations arises from the confluence of air from even opposite directions in the vicinity of a saddle-point (compare Figure 11). In contrast, the relative uncertainty at the exemplary TP at the trough's boundary is with 4.0% one order of magnitude smaller.

3.3.2. Validation of Chemical Fields

This section evaluates probabilistic ozone forecasts with respect to distributions based on meteorological and chemical analyses. The local ozone dis-

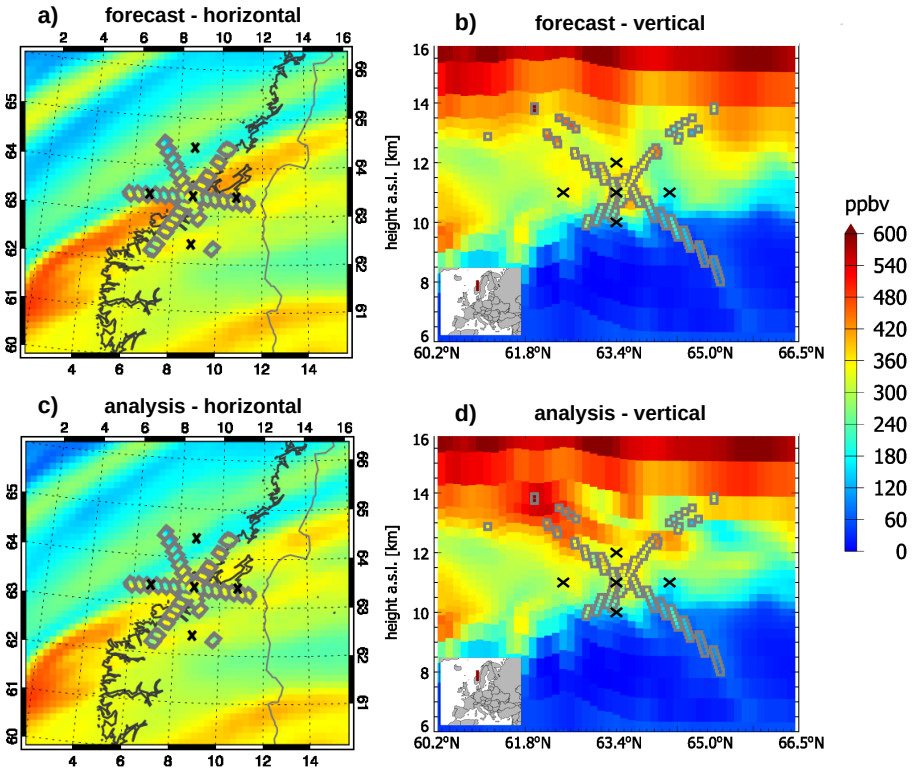

Figure 12: Forecast based on meteorological analysis (a,b) and chemical analysis using GLORIA observations (c,d) of ozone distributions at hexagonal observation on 26.09.2012 at 12 UTC in horizontal (a,c) and vertical (b,d) direction. Ozone mixing ratios are coded by color for model (contour) and GLORIA observations (gray framed boxes). Locations of source region calculations are indicated by small black crosses.

tribution forecast by the meteorological analysis is given in Figure 12a,b. The westerly shifted position of the trough induces shifted ozone filaments compared to the probabilistic forecasts. The air mass of low concentrations is located at the north-western edge where concentrations do not drop below 100 ppbv. High concentrations above 300 ppbv are predicted in the south-eastern half of the area shown. Maximum values of 400 to 450 ppbv are found within a filament in the middle of the shown area including TP *center*. The south-north aligned vertical cross section (Figure 12b) shows a small vertical extension of about 1 km of this filament around 11 km height. Somewhat lower concentrations of roughly 300 ppbv are predicted for TPs *east*, *south* and *above*. The differing source area of TP *north* (compare section 3.2.3) induce medium ozone concentrations of 200 ppbv. Lower concentrations TP *below* are caused by larger contributions from tropospheric source altitudes down to 9 km.

In addition to the validation by the meteorological analysis, available high-resolution observations from GLORIA are assimilated into the modeling system. Assimilating observed ozone concentrations provides the optimal estimation of ozone distributions in the region of interest. The assimilation-based chemical analysis shown in Figure 12c,d serves as reference for validating forecast ozone distributions.

In general, forecast ozone fields based on the meteorological analysis agree well with observed concentrations. Thus, only slight improvements of the model in 11 km are induced by the assimilation. The high concentrations within the filament around 11 km were reduced down to 300 ppbv at TP *center* according to the observations. In the vertical, most obvious analysis increments can be found in altitudes between 12 and 14 km where the analysis shows filaments with concentrations around 400 ppbv (Figure 12d). The high concentrations within these filaments indicate local downward transport of stratospheric air by tropopause folding processes. However, this process cannot be confirmed by retroplume calculations because the dynamics are not affected by the assimilation.

4. Conclusions

In this study, uncertainties of source areas of airmasses in the flow-regime of a saddle-point were investigated. Containing converging and diverging flow branches, a saddle-point can be seen a crosspoint of stable and unstable manifolds, changing characteristics forward and backward in time. Based on this, the consequences for chemical composition of the local surrounding are investigated.

A retroplume algorithm was implemented into the chemical data assimilation system EURAD-IM to track source regions of air masses. By combining this algorithm with an meteorological ensemble, probabilistic retroplumes are able to account for both, (i) the contribution of different source regions to an air mass by adjoint diffusion and (ii) the uncertainty of theses source regions with respect to forecast dynamics.

The probabilistic retroplume algorithm was applied to an air volume in the vicinity of a weak saddle-point in the Ex-UTLS. Unlike at the ridge of the polar vortex, resulting source regions show fast diverging source directions covering large parts of Europe as well as altitudes between 8 and 14 km within two days. The huge ensemble spread states a high uncertainty pointing-out low analyzability of source regions in this case.

The large uncertainty of source regions show significant effect on chemical distributions. Depending on the predicted location of the saddle-point, ozone distributions within the air volume of interest become highly variable. Local concentrations range from about 50 up to 350 ppbv at the same location indicating a relative uncertainty of more than 50%. Probabilistic retroplume calculations suggest a clear connection between these concentrations and related source regions.

In addition to the considered meteorological uncertainties, other error sources may impact the presented results. On the one hand, potential errors in the retroplume calculation may originate from the linear character of the adjoint model operator. On the other hand, chemical distributions are sensitive to the initial ozone fields which was approximated by correlation to PV. For this case study,

other uncertainties may be neglectable compared to the huge ensemble spread of source regions and chemical distributions.

Nevertheless, the probabilistic retroplume approach shows good performance in approximating uncertainties around the Ex-UTLS. Although the analyzed state was not precisely predicted by any member, the large ensemble spread indicates low analyzability of source regions inducing low predictability of chemical composition. A comparison to a location at the boundary of the trough indicates that these large uncertainties in source regions and thus chemical distributions are caused by the dynamical instability at the saddle-point.

Concerning the developed probabilistic retroplume algorithm, two major conclusions are found: (i) The extension and elongation of predicted source regions demonstrates the importance to account for adjoint diffusion in retroplume calculations. (ii) The large spread of source regions within two days states high uncertainty in the history of air masses in the vicinity of even a weak saddle-point. Hence, in case of dynamical instabilities, a deterministic view of a single source location of airmasses is not appropriate in a strict sense.

These findings indicate the benefit of probabilistic retroplumes for investigating the effect of atmospheric transport and related uncertainties. Using a larger ensemble size and more cases offers the ability of a general quantification of uncertainties induced by saddle-points in the Ex-UTLS. Furthermore, the approach can be applied to other dynamical instabilities to investigate their impact on chemical distributions. For example, the importance of turbulent processes in the planetary boundary layer motivates the use of probabilistic retroplumes for uncertainty investigation close to the surface.

Competing interests

The authors declare that they have no known competing financial interests or personal relationships that could have appeared to influence the work reported in this paper.

Acknowledgements

This work has been funded by the Helmholtz Climate Initiative REKLIM (Regional Climate Change), a joint research project of the Helmholtz Association of German research centers (HGF) under grant: REKLIM-2009-07-16. The authors are indebted to the reviewer for his very valuable comments and suggestions which help to improve the paper substantially. The authors gratefully acknowledge the computing time granted through JARA-HPC on the supercomputer JURECA [54] at Forschungszentrum Jülich. This work would not have been possible without the global meteorological data obtained from the NCEP's Global Forecasting System (GFS). A special thank go to all members of the GLORIA team especially to IEK-7 of Forschungszentrum Jülich for providing the observational data (available on the HALO database: *https://halo-db.pa.op.dlr.de/dataset/1385*).

References

[1] B. J. Hoskins, M. E. McIntyre, A. W. Robertson, On the use and significance of isentropic potential vorticity maps, Quarterly Journal of the Royal Meteorological Society 111 (470) (1985) 877–946. doi:10.1002/qj.49711147002.
URL http://dx.doi.org/10.1002/qj.49711147002

[2] E. F. Danielsen, V. A. Mohnen, Project dustorm report: ozone transport, in situ measurements, and meteorological analyses of tropopause folding, Journal of Geophysical Research (1896-1977) 82 (37) (1977) 5867–5877. arXiv:https://agupubs.onlinelibrary.wiley.com/doi/pdf/10.1029/JC082i037p05867, doi:10.1029/JC082i037p05867.
URL https://agupubs.onlinelibrary.wiley.com/doi/abs/10.1029/JC082i037p05867

[3] M. Riese, F. Ploeger, A. Rap, B. Vogel, P. Konopka, M. Dameris, P. Forster, Impact of uncertainties in atmospheric mixing on simulated utls composi-

tion and related radiative effects, Journal of Geophysical Research: Atmospheres 117 (D16), d16305. doi:10.1029/2012JD017751.
URL http://dx.doi.org/10.1029/2012JD017751

[4] M. Riese, H. Oelhaf, P. Preusse, J. Blank, M. Ern, F. Friedl-Vallon, H. Fischer, T. Guggenmoser, M. Höpfner, P. Hoor, M. Kaufmann, J. Orphal, F. Plöger, R. Spang, O. Suminska-Ebersoldt, J. Ungermann, B. Vogel, W. Woiwode, Gimballed limb observer for radiance imaging of the atmosphere (gloria) scientific objectives, Atmospheric Measurement Techniques 7 (7) (2014) 1915–1928. doi:10.5194/amt-7-1915-2014.
URL http://www.atmos-meas-tech.net/7/1915/2014/

[5] A. Gettelman, P. Hoor, L. L. Pan, W. J. Randel, M. I. Hegglin, T. Birner, The extratropical upper troposphere and lower stratosphere, REVIEWS OF GEOPHYSICS 49.

[6] J. W. Waters, L. Froidevaux, R. S. Harwood, R. F. Jarnot, H. M. Pickett, W. G. Read, P. H. Siegel, R. E. Cofield, M. J. Filipiak, D. A. Flower, et al., The earth observing system microwave limb sounder (eos mls) on the aura satellite, IEEE Transactions on Geoscience and Remote Sensing 44 (5) (2006) 1075–1092.

[7] H. Fischer, M. Birk, C. Blom, B. Carli, M. Carlotti, T. v. Clarmann, L. Delbouille, A. Dudhia, D. Ehhalt, M. Endemann, et al., Mipas: an instrument for atmospheric and climate research, Atmospheric Chemistry and Physics 8 (8) (2008) 2151–2188.

[8] J. Ungermann, J. Blank, J. Lotz, K. Leppkes, L. Hoffmann, T. Guggenmoser, M. Kaufmann, P. Preusse, U. Naumann, M. Riese, A 3-d tomographic retrieval approach with advection compensation for the air-borne limb-imager gloria, Atmospheric Measurement Techniques 4 (11) (2011) 2509–2529. doi:10.5194/amt-4-2509-2011.
URL http://www.atmos-meas-tech.net/4/2509/2011/

[9] M. Kaufmann, J. Blank, T. Guggenmoser, J. Ungermann, A. Engel, M. Ern, F. Friedl-Vallon, D. Gerber, J. U. Grooß, G. Guenther, M. Höpfner, A. Kleinert, E. Kretschmer, T. Latzko, G. Maucher, T. Neubert, H. Nordmeyer, H. Oelhaf, F. Olschewski, J. Orphal, P. Preusse, H. Schlager, H. Schneider, D. Schuettemeyer, F. Stroh, O. Suminska-Ebersoldt, B. Vogel, C. M. Volk, W. Woiwode, M. Riese, Retrieval of three-dimensional small-scale structures in upper-tropospheric/lower-stratospheric composition as measured by gloria, Atmospheric Measurement Techniques 8 (1) (2015) 81–95. doi:10.5194/amt-8-81-2015.
URL http://www.atmos-meas-tech.net/8/81/2015/

[10] L. P. Riishjgaard, On four-dimensional variational assimilation of ozone data in weather-prediction models, Quarterly Journal of the Royal Meteorological Society 122 (535) (1996) 1545–1571. doi:10.1002/qj.49712253505.
URL http://dx.doi.org/10.1002/qj.49712253505

[11] H. Elbern, A. Strunk, H. Schmidt, O. Talagrand, Emission rate and chemical state estimation by 4-dimensional variational inversion, Atmospheric Chemistry and Physics 7 (14) (2007) 3749–3769. doi:10.5194/acp-7-3749-2007.
URL http://www.atmos-chem-phys.net/7/3749/2007/

[12] E. Emili, B. Barret, S. Massart, E. Le Flochmoen, A. Piacentini, L. El Amraoui, O. Pannekoucke, D. Cariolle, Combined assimilation of iasi and mls observations to constrain tropospheric and stratospheric ozone in a global chemical transport model, Atmospheric Chemistry and Physics 14 (1) (2014) 177–198. doi:10.5194/acp-14-177-2014.
URL http://www.atmos-chem-phys.net/14/177/2014/

[13] M. Bonavita, E. Hlm, L. Isaksen, M. Fisher, The evolution of the ecmwf hybrid data assimilation system, Quarterly Journal of the Royal Meteoro-

logical Society 142 (694) (2016) 287–303. doi:10.1002/qj.2652.
URL http://dx.doi.org/10.1002/qj.2652

[14] W. Lahoz, B. Khattatov, R. Menard, Data Assimilation – Making Sense of Observations, Springer, Heidelberg, 2010.

[15] E. F. Danielsen, Stratospheric-tropospheric exchange based on radioactivity, ozone and potential vorticity, Journal of the atmospheric sciences 25 (1968) 502–518.

[16] L. P. Riishjgaard, E. Källen, On the correlation between ozone and potential vorticity for large-scale rossbywaves, Journal of Geophysical Research 102 (D7) (1997) 8793–8804.

[17] A. Ebel, H. Hass, H. Jakobs, M. Laube, M. Memmesheimer, A. Oberreuter, H. Geiss, Y.-H. Kuo, Simulation of ozone intrusion caused by tropopause fold and cut-off low, Atmospheric Environment. Part A. General Topics 25 (1991) 2131–2144. doi:10.1016/0960-1686(91)90089-P.

[18] G. Ancellet, M. Beekmann, A. Papayannis, Impact of a cutoff low development on downward transport of ozone in the troposphere, Journal of Geophysical Research: Atmospheres 99 (D2) (1994) 3451–3468. arXiv:https://agupubs.onlinelibrary.wiley.com/doi/pdf/10.1029/93JD02551, doi:10.1029/93JD02551.
URL https://agupubs.onlinelibrary.wiley.com/doi/abs/10.1029/93JD02551

[19] L. Riishjgaard, A direct way of specifying flow-dependent background error correlations for meteorological analysis systems, Tellus series A-dynamic meteorology ans oceanography 50A (1998) 42–57.

[20] H. Elbern, J. Hendricks, A. Ebel, A climatology of tropopause folds by global analyses, Theoretical and Applied Climatology 59 (3) (1998) 181–200. doi:10.1007/s007040050023.
URL https://doi.org/10.1007/s007040050023

[21] A. R. Douglass, R. B. Rood, R. S. Stolarski, M. R. Schoeberl, M. H. Proffitt, J. J. Margitan, M. Loewenstein, J. R. Podolske, S. E. Strahan, Global three-dimensional constituent fields derived from profile data, Geophysical Research Letters 17 (4) (1990) 525–528. doi:10.1029/GL017i004p00525.
URL http://dx.doi.org/10.1029/GL017i004p00525

[22] D. J. Lary, M. P. Chipperfield, J. A. Pyle, W. A. Norton, L. P. Riishjgaard, Three-dimensional tracer initialization and general diagnostics using equivalent pv latitudepotential-temperature coordinates, Quarterly Journal of the Royal Meteorological Society 121 (521) (1995) 187–210. doi:10.1002/qj.49712152109.
URL http://dx.doi.org/10.1002/qj.49712152109

[23] K. P. Bowman, L. L. Pan, T. Campos, R. Gao, Observations of fine-scale transport structure in the upper troposphere from the high-performance instrumented airborne platform for environmental research, Journal of Geophysical Research: Atmospheres 112 (D18). arXiv:https://agupubs.onlinelibrary.wiley.com/doi/pdf/10.1029/2007JD008685, doi:10.1029/2007JD008685.
URL https://agupubs.onlinelibrary.wiley.com/doi/abs/10.1029/2007JD008685

[24] A. Stohl, M. Hittenberger, G. Wotawa, Validation of the lagrangian particle dispersion model flexpart against large-scale tracer experiment data, Atmospheric Environment 32 (24) (1998) 4245 – 4264. doi:https://doi.org/10.1016/S1352-2310(98)00184-8.
URL http://www.sciencedirect.com/science/article/pii/S1352231098001848

[25] R. Draxier, G. Hess, An overview of the HYSPLIT_4 modelling system for trajectories, dispersion and deposition, AUSTRALIAN METEOROLOGICAL MAGAZINE 47 (4) (1998) 295–308.

[26] K. S. Rao, Source estimation methods for atmospheric dispersion, Atmospheric Environment 41 (33) (2007) 6964 – 6973. doi:https://doi.org/10.1016/j.atmosenv.2007.04.064.
URL http://www.sciencedirect.com/science/article/pii/S1352231007004086

[27] A. Baklanov, A. Aloyan, A. Mahura, V. Arutyunyan, P. Luzan, Evaluation of sourcereceptor relationship for atmospheric pollutants using approaches of trajectory modelling, cluster, probability fields analyses and adjoint equations, Atmospheric Pollution Research 2 (4) (2011) 400 – 408. doi:https://doi.org/10.5094/APR.2011.045.
URL http://www.sciencedirect.com/science/article/pii/S1309104215304669

[28] B. Vogel, G. Günther, R. Müller, J.-U. Grooß, P. Hoor, M. Krämer, S. Müller, A. Zahn, M. Riese, Fast transport from southeast asia boundary layer sources to northern europe: rapid uplift in typhoons and eastward eddy shedding of the asian monsoon anticyclone, Atmospheric Chemistry and Physics 14 (23) (2014) 12745–12762. doi:10.5194/acp-14-12745-2014.
URL https://www.atmos-chem-phys.net/14/12745/2014/

[29] A. Stohl, Computation, accuracy and applications of trajectoriesa review and bibliography, Atmospheric Environment 32 (6) (1998) 947 – 966. doi:https://doi.org/10.1016/S1352-2310(97)00457-3.
URL http://www.sciencedirect.com/science/article/pii/S1352231097004573

[30] K. Khanin, Quasi-periodic motions of vortex systems, Physica D: Nonlinear Phenomena 4 (2) (1982) 261 – 269. doi:https://doi.org/10.1016/0167-2789(82)90067-7.
URL http://www.sciencedirect.com/science/article/pii/0167278982900677

[31] C. Marchioro, M. Pulvirenti, Vortex models in two-dimensional fluid dynamics, Springer, Berlin, 1984.

[32] P. K. Newton, The N-vortex problem: Analytical techniques, Springer, New York, 2001.

[33] S. L. Ziglin, Nonintegrability of a problem on the motion of four point vortices, Soviet. Math. Dokl. 21 (1) (1980) 296–299.

[34] W. M. Oliva, On the chaotic behavior and the nonintegrability of the 4 vortices problem, Annales de l Institut Henri Poincare - Physique Theorique 55 (2) (1991) 707–718.

[35] J. T. Merrill, R. Bleck, L. Avila, Modeling atmospheric transport to the marshall islands, Journal of Geophysical Research: Atmospheres 90 (D7) (1985) 12927–12936. arXiv:https://agupubs.onlinelibrary.wiley.com/doi/pdf/10.1029/JD090iD07p12927, doi:10.1029/JD090iD07p12927.
URL https://agupubs.onlinelibrary.wiley.com/doi/abs/10.1029/JD090iD07p12927

[36] J. W. Bergman, E. J. Jensen, L. Pfister, T. V. Bui, Air parcel trajectory dispersion near the tropical tropopause, Journal of Geophysical Research: Atmospheres 121 (8) (2016) 3759–3775.

[37] S. K. Singh, M. Sharan, J.-P. Issartel, Inverse modelling methods for identifying unknown releases in emergency scenarios: an overview, International Journal of Environment and Pollution 57 (1-2) (2015) 68–91.

[38] M. Bocquet, H. Elbern, H. Eskes, M. Hirtl, R. Žabkar, G. R. Carmichael, J. Flemming, A. Inness, M. Pagowski, J. L. Pérez Camaño, P. E. Saide, R. San Jose, M. Sofiev, J. Vira, A. Baklanov, C. Carnevale, G. Grell, C. Seigneur, Data assimilation in atmospheric chemistry models: current status and future prospects for coupled chemistry meteorology models, Atmospheric Chemistry and Physics 15 (10) (2015) 5325–5358. doi:

10.5194/acp-15-5325-2015.
URL https://www.atmos-chem-phys.net/15/5325/2015/

[39] F. Hourdin, O. Talagrand, Eulerian backtracking of atmospheric tracers. i: Adjoint derivation and parametrization of subgrid-scale transport, Quarterly Journal of the Royal Meteorological Society 132 (615) (2006) 567–583. arXiv:https://rmets.onlinelibrary.wiley.com/doi/pdf/10.1256/qj.03.198.A, doi:10.1256/qj.03.198.A.
URL https://rmets.onlinelibrary.wiley.com/doi/abs/10.1256/qj.03.198.A

[40] W. C. Skamarock, J. B. Klemp, J. Dudhia, D. O. Gill, D. M. Barker, W. Wang, J. G. Powers, A description of the advanced research wrf version 2, NCAR technical note.

[41] H. J. Hass, H.and Jakobs, M. Memmesheimer, Analysis of a regional model (eurad) near surface gas concentration predictions using observations from networks, Meteorology and Atmospheric Physics 57 (1) (1995) 173–200. doi:10.1007/BF01044160.
URL http://dx.doi.org/10.1007/BF01044160

[42] W. R. Stockwell, F. Kirchner, M. Kuhn, S. Seefeld, A new mechanism for regional atmospheric chemistry modeling, Journal of Geophysical Research: Atmospheres 102 (D22) (1997) 25847–25879. arXiv:https://agupubs.onlinelibrary.wiley.com/doi/pdf/10.1029/97JD00849, doi:10.1029/97JD00849.
URL https://agupubs.onlinelibrary.wiley.com/doi/abs/10.1029/97JD00849

[43] I. J. Ackermann, H. Hass, M. Memmesheimer, A. Ebel, F. S. Binkowski, U. Shankar, Modal aerosol dynamics model for europe: development and first applications, Atmospheric Environment 32 (17) (1998) 2981 – 2999. doi:https://doi.org/10.1016/S1352-2310(98)00006-5.

URL http://www.sciencedirect.com/science/article/pii/S1352231098000065

[44] P. Courtier, Dual formulation of four-dimensional variational assimilation, Quarterly Journal of the Royal Meteorological Society 123 (544) (1997) 2449–2461. doi:10.1002/qj.49712354414.
URL http://dx.doi.org/10.1002/qj.49712354414

[45] D. C. Liu, J. Nocedal, On the limited memory bfgs method for large scale optimization, Mathematical Programming 45 (1) (1989) 503–528. doi:10.1007/BF01589116.
URL http://dx.doi.org/10.1007/BF01589116

[46] R. N. Bannister, A review of forecast error covariance statistics in atmospheric variational data assimilation. ii: Modelling the forecast error covariance statistics, Quarterly Journal of the Royal Meteorological Society 134 (637) (2008) 1971–1996. doi:10.1002/qj.340.
URL http://dx.doi.org/10.1002/qj.340

[47] F. dOvidio, E. Shuckburgh, B. Legras, Local mixing events in the upper troposphere and lower stratosphere. part i: Detection with the lyapunov diffusivity, Journal of the Atmospheric Sciences 66 (12) (2009) 3678–3694. doi:10.1175/2009JAS2982.1.
URL https://doi.org/10.1175/2009JAS2982.1

[48] H. Elbern, J. Schwinger, R. Botchorishvili, Chemical state estimation for the middle atmosphere by four-dimensional variational data assimilation: System configuration, Journal of Geophysical Research 115 (D6) (2010) D06302+. doi:10.1029/2009jd011953.
URL http://dx.doi.org/10.1029/2009jd011953

[49] J. Ungermann, J. Blank, M. Dick, A. Ebersoldt, F. Friedl-Vallon, A. Giez, T. Guggenmoser, M. Höpfner, T. Jurkat, M. Kaufmann, S. Kaufmann, A. Kleinert, M. Krämer, T. Latzko, H. Oelhaf, F. Olchewski, P. Preusse,

C. Rolf, J. Schillings, O. Suminska-Ebersoldt, V. Tan, N. Thomas, C. Voigt, A. Zahn, M. Zöger, M. Riese, Level 2 processing for the imaging fourier transform spectrometer gloria: derivation and validation of temperature and trace gas volume mixing ratios from calibrated dynamics mode spectra, Atmospheric Measurement Techniques 8 (6) (2015) 2473–2489. doi:10.5194/amt-8-2473-2015.
URL http://www.atmos-meas-tech.net/8/2473/2015/

[50] T. M. Hamill, G. T. Bates, J. S. Whitaker, D. R. Murray, M. Fiorino, T. J. Galarneau, Y. Zhu, W. Lapenta, Noaa's second-generation global medium-range ensemble reforecast dataset, Bulletin of the American Meteorological Society 94 (10) (2013) 1553–1565. arXiv:https://doi.org/10.1175/BAMS-D-12-00014.1, doi:10.1175/BAMS-D-12-00014.1.
URL https://doi.org/10.1175/BAMS-D-12-00014.1

[51] C. J. Walcek, Minor flux adjustment near mixing ratio extremes for simplified yet highly accurate monotonic calculation of tracer advection, Journal of Geophysical Research: Atmospheres 105 (D7) (2000) 9335–9348. arXiv:https://agupubs.onlinelibrary.wiley.com/doi/pdf/10.1029/1999JD901142, doi:10.1029/1999JD901142.
URL https://agupubs.onlinelibrary.wiley.com/doi/abs/10.1029/1999JD901142

[52] E. F. Danielsen, R. S. Hipskind, S. E. Gaines, G. W. Sachse, G. L. Gregory, G. F. Hill, Three-dimensional analysis of potential vorticity associated with tropopause folds and observed variations of ozone and carbon monoxide, Journal of Geophysical Research: Atmospheres 92 (D2) (1987) 2103–2111. doi:10.1029/JD092iD02p02103.
URL http://dx.doi.org/10.1029/JD092iD02p02103

[53] T. N. Rao, S. Kirkwood, J. Arvelius, P. von der Gathen, R. Kivi, Climatology of utls ozone and the ratio of ozone and potential vorticity over northern europe, Journal of Geophysical Research: Atmospheres

108 (D22). arXiv:https://agupubs.onlinelibrary.wiley.com/doi/pdf/10.1029/2003JD003860, doi:10.1029/2003JD003860.
URL https://agupubs.onlinelibrary.wiley.com/doi/abs/10.1029/2003JD003860

[54] Jülich Supercomputing Centre, JURECA: Modular supercomputer at Jülich Supercomputing Centre, Journal of large-scale research facilities 4 (A132). doi:10.17815/jlsrf-4-121-1.
URL http://dx.doi.org/10.17815/jlsrf-4-121-1